JTTEE5 17:646–654
DOI: 10.1007/s11666-008-9238-5
1059-9630/$19.00 © ASM International

Peer Reviewed

The Effect of Undercooling on Solidification of YSZ Splats

Haibo Liu, Markus Bussmann, and Javad Mostaghimi

(Submitted May 21, 2008; in revised form September 2, 2008)

We consider the rapid solidification of a molten YSZ particle, by solving the so-called hyperbolic equations for heat and mass transfer. The hyperbolic model predicts the interface undercooling (due to thermal and solutal effects) and velocity as a function of time, as well as the yttria redistribution within the solid phase. Results are then compared to corresponding ones that we obtained from a parabolic model, to assess the extent to which YSZ solidification is influenced by nonequilibrium effects. Results indicate that these effects are limited to the early part of the solidification process when undercooling is most significant. At this stage, the interface velocity is unsteady, and solute redistribution is most evident. As solidification decelerates, the nonequilibrium effects wane and solidification can then be properly modeled as an equilibrium process.

Keywords hyperbolic, interface tracking, nonequilibrium, rapid solidification, relaxation time, undercooling, YSZ

1. Introduction

Thermal spray coating is an enabling technology, which has wide application in many industries including the gas turbine, aerospace, automotive, and biomedical (Ref 1). Zirconia-based ceramic coatings in particular are used as effective thermal barriers for metal structures in gas turbines (Ref 2, 3). These coatings can delay thermally induced failure, thus increasing the durability of machine components.

In the plasma spray process, yttria-stabilized zirconia (YSZ) powders are injected into a plasma jet, particles melt and accelerate until they collide with a substrate, spread, and solidify. The substrate material can vary, depending on use. Deposition of high quality coatings requires knowledge that involves materials and interface science, fluid mechanics, and heat transfer. This multidisciplinary character of the spray coating process implies that the development of new products and techniques requires a high investment. The simulation of spray coating formation can help optimize a design, and so save time and money.

This article is an invited paper selected from presentations at the 2008 International Thermal Spray Conference and has been expanded from the original presentation. It is simultaneously published in *Thermal Spray Crossing Borders, Proceedings of the 2008 International Thermal Spray Conference*, Maastricht, The Netherlands, June 2-4, 2008, Basil R. Marple, Margaret M. Hyland, Yuk-Chiu Lau, Chang-Jiu Li, Rogerio S. Lima, and Ghislain Montavon, Ed., ASM International, Materials Park, OH, 2008.

Haibo Liu, Markus Bussmann, and **Javad Mostaghimi**, Department of Mechanical and Industrial Engineering and Centre for Advanced Coating Technologies, University of Toronto, 5 King's College Road, Toronto, ON, Canada M5S 3G8. Contact e-mail: bussmann@mie.utoronto.ca.

List of Symbols

C	concentration (wt.%)
C_0	initial concentration (wt.%)
C_p	specific heat capacity (J kg^{-1} K^{-1})
b	splat thickness (m)
D	mass diffusivity (m^2 s^{-1})
h	heat transfer coefficient (W m^{-2} K^{-1})
J_C	concentration flux (wt.% m s^{-1})
k_f	nonequilibrium partition coefficient
k_e	equilibrium partition coefficient
m	slope of nonequilibrium liquidus (K wt.%$^{-1}$)
m_e	slope of equilibrium liquidus (K wt.%$^{-1}$)
Q	latent heat of solidification (J kg^{-1})
T	temperature (K)
T_m	equilibrium melting temperature (K)
T_0	initial temperature (K)
V_D	mass diffusion velocity (m s^{-1})
V_i	interface velocity (m s^{-1})

Greek Symbols

α	thermal diffusivity (m^2 s^{-1})
κ	thermal conductivity (W m^{-1} K^{-1})
μ	linear kinetics coefficient (m s^{-1} K^{-1})
ρ	density (kg m^{-3})
τ	relaxation time (s)

Subscripts and Superscripts

i	interface
j	solid or liquid phase
−	liquid interface
+	solid interface

Pure zirconia has a complex allotropic structure (Ref 4). A cubic crystal structure exists between 2400 and 2700 K; it then transforms into a tetragonal structure as it further cools. When the temperature reaches about 1000 K, the tetragonal crystals transform to monoclinic form. This phase transformation involves volume change that may cause compression or tension in the coating, which can induce surface cracking and poor mechanical flexibility. To circumvent these problems, a zirconia yttria (6-8 wt.%) mixture, which has no transformation to a monoclinic phase at low temperature is used. Further, research (Ref 4) has found that when rapidly solidified, the zirconia-rich corner of the phase diagram has a tetragonal-prime phase, which is meta-stable.

Few numerical studies of the rapid solidification of YSZ have been published (Ref 2). Pure metal models are only useful in conditions far different from those of ceramic solidification (e.g., Ref 5), and so here we solve the coupled thermal and concentration equations for a binary system. Also, Fourier's model is usually used to simulate heat conduction during solidification, but this model is only appropriate for relatively slow processes. To solve a rapid solidification problem, this so-called parabolic model should be replaced by a hyperbolic one, by adding a relaxation term to Fourier's model to take into account nonequilibrium effects related to the interface velocity-induced heat wave (Ref 6). Using a similar strategy based on the theory of so-called extended irreversible thermodynamics, Sobolev (Ref 7) added the relaxation term to the equilibrium equation for concentration diffusion, to model alloy solidification as a hyperbolic process. And to simplify the problem, Sobolev and Galenko assumed a constant interface velocity at the solidification front, and so were able to obtain analytic solutions for planar and dendritic interfaces (Ref 7, 8, 9).

Numerical models of spray coating consider a single droplet, or a spray of them, impacting the surface of a substrate. As the droplet contacts the surface, heat is released that fluxes into the substrate; grains begin to grow when nuclei are beyond the critical size of heterogeneous nucleation. The microstructure of a spray coating, including the grain shape, density, and orientation, is affected by the interface velocity (Ref 2), which is determined via an extra undercooling constraint (Ref 2, 5).

Nonequilibrium effects associated with the relaxation term occur if the solid/liquid interface velocity is comparable to the diffusive speed (Ref 7). Determining an accurate interface velocity profile can help to explain the microstructure of a solidified material. The interface velocity also affects the splat morphology, as it has been observed that splat structure can vary with the substrate temperature. Note that an important factor that affects the solidification speed is the change of thermal contact resistance with temperature. For metal substrates, thermal contact resistance increases with increasing substrate temperature, because the oxide layer formed at the surface becomes thicker. For nonmetal surfaces, the situation is reversed, due to the desorption of adsorbed gases on the surface. Figure 1 shows YSZ splats deposited on stainless steel at different temperatures, and illustrates how the change in substrate temperature and thus thermal contact resistance affects the spread time and the cooling rate of the splats, and thus the overall splat morphology. Similar experiments were conducted by Bianchi et al. (Ref 10) and Fukomoto et al. (Ref 11), who presented scanning electron micrographs of individual alumina and zirconia splats deposited by plasma spraying on a stainless steel

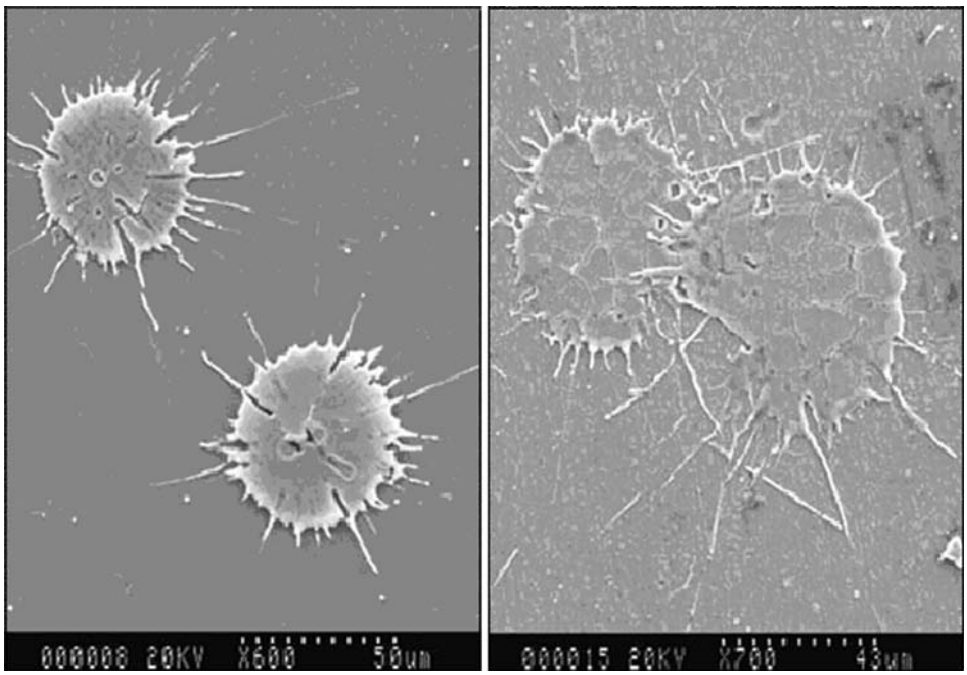

Fig. 1 Single YSZ splats on a polished stainless steel substrate at (a) 300 °C and (b) 600 °C

plate. They found that droplets landing on a cold substrate were more irregular in shape, with fingers radiating out from their centers, while droplets that landed on a hot substrate were usually shaped like disks. They explained that the solidified layer next to the substrate triggers radial jetting of the liquid and so leads to splashing (Ref 12). Therefore, the faster the interface velocity, the faster the solid layer forms, and the more likely the splat will splash. This explanation suggests that interface velocity can affect the morphology of a splat. The interface velocity also can affect the splat microstructure. According to the grain formation model of Kurz and Fisher (Ref 13), the morphology, tip radius, and cell and dendrite spacings are all closely related to interface velocity. Therefore, determining an accurate interface velocity enables us to analyze splat morphology. The interface tracking model (Ref 5, 14) we present here, for the rapid solidification of YSZ, yields an accurate interface velocity profile.

At the splat/substrate interface, it is well known that the interface velocity of the solidification front is strongly affected by the substrate temperature (Ref 12) as well as by the condition of the substrate (e.g., contamination (Ref 15), oxidation (Ref 16), roughness (Ref 17)). To simplify our simulation, these effects are represented by two parameters that we varied: the surface temperature and a heat transfer coefficient.

To calculate the local yttria concentration at the interface, the kinetic solute partition function k_f is a critical coefficient. k_f is the ratio of the solute concentration on the solid side of the dynamic solidification front to the concentration on the liquid side. The concentration difference at the solid/liquid interface is what drives solute redistribution. k_e is the ratio of the equilibrium solidus to liquidus concentrations based on the phase diagram. At high interface velocity, k_f deviates from k_e. Aziz (Ref 18, 19) derived an expression for k_f via a continuous growth model that assumes a ''rough interface'' that provides sites for crystallization events (Ref 19); Sobolev and Galenko (Ref 7, 9) extended this expression to obtain a nonequilibrium partition coefficient based on a modified Fick's law.

Another coefficient that affects the local yttria concentration at the interface is the slope of the liquidus m. m_e is the equilibrium liquidus slope based on the phase diagram. At higher interface velocities, m deviates from m_e. Aziz and Boettinger (Ref 19) obtained the slope of the nonequilibrium liquidus by expressing a chemical potential balance of a binary concentration system, from which the total Gibbs free energy could be expressed; as with k_f, Galenko (Ref 9) extended the expression for m to include hyperbolic effects.

Both physical and mathematical complications of a binary rapid solidification process lead to equations that are challenging to solve numerically and theoretically. Wang (Ref 14) simulated planar rapid solidification using an interface tracking method, but solved the parabolic rather than the hyperbolic equations. Sobolev and Galenko (Ref 7, 9) solved the hyperbolic equations analytically; they obtained a steady-state solution by assuming a constant interface velocity. For this work, we implemented the iterative interface tracking method of Wang (Ref 14), which is both accurate and efficient, but applied the methodology to solve the hyperbolic equations to predict solidification characteristics that include the solid/liquid interface velocity, temperature, and the partition coefficient. This information in turn can be used to interpret experimental results such as those illustrated in Fig. 1.

2. Physical Model and Methodology

To solve for the nonequilibrium phase change of YSZ rapidly solidifying on a substrate, we have extended the 1D model of Wang (Ref 14), based on the following assumptions and idealizations:

1. an impacting droplet rapidly forms a thin layer of molten YSZ, with uniform initial temperature; the droplet is assumed to spread rapidly so that solidification can be modeled as a 1D phenomena; the validity of this assumption depends on the particular parameters of the droplet impact, but given the complexity of the heat and mass transfer analysis presented here and the focus on solidification just above the substrate, an analysis that also incorporates flow would make the problem intractable;
2. the interface velocity is linearly related to the undercooling;
3. the droplet and substrate are in contact along a stable planar interface, and the heat transfer coefficient at the droplet/substrate interface is assumed to be constant, inferred from experimental measurements;
4. the heat transfer coefficient at the upper surface of the splat is much smaller than that at the droplet/substrate interface, and so we assume it to be zero.

Fick's First Law states that the flux of a component across a concentration field is proportional to the concentration gradient, and so assumes an infinite velocity of concentration propagation:

$$J_c + D_j \nabla C_j = 0 \qquad \text{(Eq 1)}$$

where C is the concentration of the solute, D is the solute diffusivity, J_c is the diffusion mass flux, and the subscript j represents the solid or liquid phase. Diffusion of a dissolved component in a solid or liquid phase can be expressed as a concentration balance:

$$\nabla \cdot J_c + \frac{\partial C_j}{\partial t} = 0 \qquad \text{(Eq 2)}$$

where t is time. It is important to note that the above equations assume microscopic reversibility, which means that the concentration flux is uniquely linked to diffusion, and that the inertial effects of the concentration flux acceleration are ignored. Namely, a signal change at one point anywhere in a concentration field will instantaneously be felt everywhere else. The above equations accurately predict most experimental results. However, when mass transport is relatively high, the relaxation time to accelerate the mass flux will be relatively large; in such a case, a relaxation term should be included in the transport equation.

Cattaneo (Ref 20) first proposed a damped version of Fourier's heat conduction law in 1948. In the case of mass transport, a modified Fick's law can be expressed in a similar way. It includes a mass flux relaxation term that involves a relaxation time τ_D (Ref 5). In a local nonequilibrium situation, τ_D is the time interval necessary for atoms to jump onto a neighboring lattice, and thus for the mass flux to reach a stable state.

Adding a relaxation term to Fick's First Law yields a general Fick's Law (Ref 9):

$$\tau_D \frac{\partial J_c}{\partial t} + J_c + D_j \nabla C_j = 0 \quad \text{(Eq 3)}$$

where $\tau_D = D_j/V_D{}^2$ (Ref 21). According to previous work on pure metal solidification (Ref 5), in which we solved only for the thermal field, a value of τ_κ (the thermal equivalent of τ_D) on the order of 10^{-9} s yielded negligible differences between the parabolic and hyperbolic models. But as YSZ has a relatively low mass diffusivity and a low diffusive speed $V_D \sim 1$ m s^{-1} (Ref 22), τ_D for the concentration equation is also on the order of 10^{-9} s, yet one would expect a more dramatic effect of this term. Also, the solute partition coefficient and the liquidus slope are both related to V_D, which led us to investigate the effect of τ_D on the solidification of YSZ.

To analyze the extent of nonequilibrium behavior is to compare the magnitudes of the solid/liquid normal interface velocity V_i and the diffusive speed V_D of the melt. When V_i is comparable to but smaller than V_D, the diffusive velocity cannot be assumed to be infinite. Solute propagation is then a joint process of diffusion and wave propagation (Ref 7). As $V_i \to V_D$, the wave mechanism dominates. When $V_i > V_D$, diffusion in the liquid ceases, and solidification is then unrelated to the concentration distribution. Hence, the extent of nonequilibrium behavior is related to the magnitudes of V_i and V_D: if these velocities are comparable, then concentration-induced nonequilibrium effects will be more pronounced.

Combining the above equations, a hyperbolic equation for the concentration is obtained (Ref 7):

$$\frac{\partial C_j}{\partial t} + \tau_D \frac{\partial^2 C_j}{\partial t^2} = D_j \nabla^2 C_j \quad \text{(Eq 4)}$$

and a hyperbolic heat conduction equation can be expressed similarly:

$$\frac{\partial T_j}{\partial t} + \tau_\kappa \frac{\partial^2 T_j}{\partial^2 t} = \alpha_j \nabla^2 T_j \quad \text{(Eq 5)}$$

where α_j is the thermal diffusivity, T is the temperature, and τ_κ represents the time lag between the temperature gradient and the commencement of heat flow in a medium. Here we assume this thermal time lag is also associated with the time required for atoms to jump from the liquid side to the solid side, and so we assume τ_κ and τ_D to be the same. This model, then, describes heat wave propagation with finite velocity. But, as already noted, τ_κ in its proper range will have little effect on the thermal field, and so although we assume τ_κ and τ_D to be equal, we expect differences between the parabolic and hyperbolic models to result from the concentration equation.

At the solid/liquid interface we impose an extra constraint on the governing equations (Ref 2):

$$T_i = T_m + m \cdot C_i^- - V_i/\mu \quad \text{(Eq 6)}$$

where μ is the kinetic coefficient of interface motion, T_m is the equilibrium melting temperature, and C_i^- is the interface concentration on the liquid side. Because we assume a planar interface, there is no curvature-induced undercooling.

The magnitude of nonequilibrium effects depends on V_i. As $V_i \to V_D$, the local concentration at the interface is affected, because the magnitude of the concentration flux at the interface is dominated by the wave mechanism instead of by species diffusion. As $V_i \to V_D$, partitionless phenomena occur, and a generalized partition function for solute portioning is required. Meanwhile the liquidus curve on the phase diagram is shifted because of solute trapping, which requires the use of a generalized form of the liquidus slope to consider such a shift. The generalized equations for the partition coefficient and for the liquidus slope are presented below.

Regarding the temperature field, local thermal equilibrium of an alloy is established much more quickly than the local equilibrium of the diffusion field, to the extent that Galenko (Ref 21) ignored the thermal nonequilibrium term in the governing equations. In our simulations, we keep the nonequilibrium term, but we ignore the nonequilibrium thermal effects (Ref 5). However, as the dynamic interface condition (Eq 6) is a constraint on the hyperbolic governing equations (Eq 4, 5), the temperature field is still affected by hyperbolic effects.

At the interface, the concentration undercooling is given by Eq 6. To calculate the concentration at the planar interface, the concentration segregation

$$C_i^+ = k_f C_i^- \quad \text{(Eq 7)}$$

is required (C_i^+ is the interface concentration on the solid side), and k_f is the nonequilibrium partition coefficient, expressed by Aziz et al. (Ref 18, 19) as:

$$k_f = \frac{k_e + V_i/V_D}{1 + V_i/V_D} \quad \text{(Eq 8)}$$

where k_e is the equilibrium partition coefficient.

By introducing an effective diffusion coefficient $D^* = \left(1 - \frac{V_i^2}{V_D}\right)$ for $V_i < V_D$ and following the derivation of Aziz (Ref 18, 19), Sobolev and Galenko (Ref 7, 9) obtained a more general partition coefficient:

$$k_f = \frac{k_e(1 - V_i^2/V_D^2) + V_i/V_D}{1 - V_i^2/V_D^2 + V_i/V_D}, \quad V_i < V_D \quad \text{(Eq 9)}$$

and

$$k_f = 1, \quad V_i \geq V_D \quad \text{(Eq 10)}$$

since solute is then completely trapped. Both expressions for k_f (Eq 8, 9, 10) have been used previously by researchers investigating rapid solidification.

In Eq 6, the nonequilibrium liquidus slope m is also unknown. Based on arguments described in the Introduction, Aziz and Boettinger derived the following expression:

$$m = m_e[1 + (k_e - k_f(1 - \ln(k_f/k_e))/(1 - k_e)] \quad \text{(Eq 11)}$$

where m_e is the slope of the equilibrium liquidus. An alternative expression for m was derived by Galenko (Ref 9) based on the hyperbolic model; adding a diffusion relaxation term to the steady diffusion flux leads to:

$$m = \frac{m_e}{1 - k_e}\left[1 - k_f + \ln(k_f/k_e) + (1 - k_f)^2(V_i/V_D)\right], \quad V_i < V_D \quad \text{(Eq 12)}$$

$$m = \frac{m_e \ln k_e}{k_e - 1}, \quad V_i \geq V_D \quad \text{(Eq 13)}$$

As for k_f, both expressions for m (Eq 11-13) have been used to investigate rapid solidification.

All that remains is to specify the initial and boundary conditions. The initial conditions are:

$$T(x,0) = T_0, \quad C(x,0) = C_0, \quad J(x,0) = J_C(x,0) = 0 \quad \text{(Eq 14)}$$

At the upper surface of the splat ($x = b$):

$$\frac{\partial T(b,t)}{\partial x} = 0, \quad \frac{\partial C(b,t)}{\partial x} = 0 \quad \text{(Eq 15)}$$

At the base of the splat, we simplify the thermal boundary condition (Ref 5), and assume no mass transfer:

$$J^+ = h[T(x,0) - T_\infty], \quad \frac{\partial C(0,t)}{\partial x} = 0 \quad \text{(Eq 16)}$$

where T_∞ is a specified substrate temperature, δy is the thickness of the solidified layer, and h is the heat transfer coefficient. Since the mass diffusivity on the solid side is several orders of magnitude less than on the liquid side, we ignore concentration diffusion in the solid.

At the moving solid/liquid interface the following is an expression of energy conservation:

$$T_Q \cdot V_i = J^- - J^+ \quad \text{(Eq 17)}$$

where $T_Q = Q \cdot C_p^{-1}$ is the temperature of adiabatic solidification, Q is the latent heat, C_p is the specific heat, and J^- and J^+ represent the heat fluxes from the liquid and solid sides of the solidification front.

The corresponding conservation equation for concentration at the solid/liquid interface is the following flux balance:

$$\left(C_i^- - C_i^+\right) \cdot V_i = J_C^- - J_C^+ \quad \text{(Eq 18)}$$

where C_i^- and C_i^+ are the concentrations on the liquid and solid sides of the solidification front, and J_C^- and J_C^+ represent the corresponding fluxes.

Finally, at the solid/liquid interface, the expressions for k_f and m derived both by Aziz (Eq 8, 11) and by Galenko (Eq 9, 10, 12, 13) were applied to solve the parabolic and hyperbolic sets of equations, respectively.

By assuming that solidification begins when the interface temperature between the splat and substrate reaches the nucleation temperature (below the equilibrium melting temperature), the interface velocity is then linearly related to the local undercooling via a crystal growth kinetics relationship (Eq 6), which is an extra constraint on the governing equations (Eq 4, 5).

To solve the system of equations numerically, a common solution strategy was applied. Rather than solve concentration Eq 4, we solve Eq 2 and 3, which are two first-order partial differential equations, as well as Eq 5. We fix the moving solid/liquid interface by transforming the physical coordinate x to a computational one η (see Fig. 2):

$$\eta = \left(\frac{x}{\varepsilon}\right)^p \quad \text{(Eq 19)}$$

p adjusts the mesh density in the liquid region (Ref 5); this non-uniform transformation is necessary to solve the system efficiently. The governing equations in the computational domain ($0 \leq \eta \leq 1$) are then the following:

$$\frac{\partial C}{\partial t} - p\frac{d\varepsilon}{dt}\frac{\partial C}{\partial \eta} + p\eta^{\left(\frac{p-1}{p}\right)}\frac{1}{\varepsilon}\frac{\partial J_c}{\partial \eta} = 0 \quad \text{(Eq 20)}$$

$$\tau_D\frac{\partial J_c}{\partial t} - \tau_D p\frac{\eta}{\varepsilon}\frac{d\varepsilon}{dt}\frac{\partial J_c}{\partial \eta} + J_c + p\eta^{\left(\frac{p-1}{p}\right)}\frac{D}{\varepsilon}\frac{\partial C}{\partial \eta} = 0 \quad \text{(Eq 21)}$$

$$\rho c\frac{\partial T}{\partial t} - \rho c p\frac{d\varepsilon}{dt}\frac{\partial T}{\partial \eta} + p\eta^{\left(\frac{p-1}{p}\right)}\frac{1}{\varepsilon}\frac{\partial J}{\partial \eta} = 0 \quad \text{(Eq 22)}$$

$$\tau_D\frac{\partial J}{\partial t} - \tau_D p\frac{\eta}{\varepsilon}\frac{d\varepsilon}{dt}\frac{\partial J}{\partial \eta} + J + p\eta^{\left(\frac{p-1}{p}\right)}\frac{\kappa}{\varepsilon}\frac{\partial T}{\partial \eta} = 0 \quad \text{(Eq 23)}$$

MacCormack's predictor-corrector scheme was used to solve this set of equations: at each time step, we iteratively solved for a V_i that also satisfied the thermal and mass conservation conditions at the interface (Ref 5).

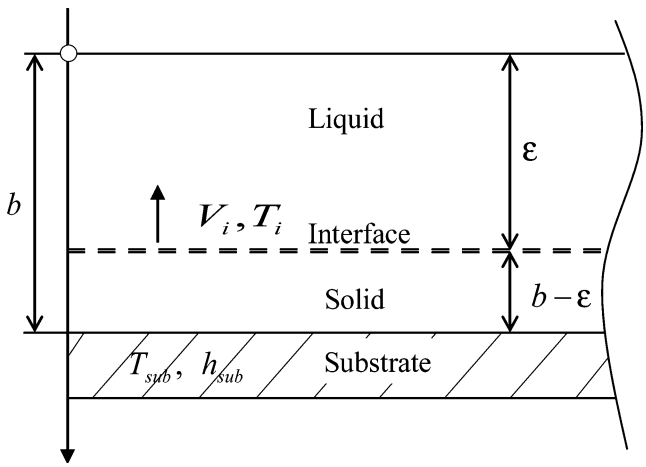

Fig. 2 Schematic of the geometry and coordinate system used in the numerical simulations (Ref 5)

3. Results and Discussion

The physical properties of YSZ (Ref 2, 4, 22) used in these simulations are specified in Table 1. YSZ has a relatively low thermal conductivity and thus a low diffusive speed $V_D \sim 1.0$ m s^{-1}, which is why we solve the hyperbolic heat and concentration equations, although we also solved the parabolic equations, and compared the results. At the melt/substrate interface, we specified a heat transfer coefficient $h = 1.0 \times 10^7$ or 5.0×10^7 W m^{-2} K^{-1} (Ref 2). The substrate temperature was maintained at a constant 500 K.

To solve the concentration equation we used 1000 nodes, concentrated near the solid/liquid interface to resolve the concentration gradient. We required only 100 nodes distributed uniformly to solve the energy equation over the same domain. The equilibrium melting temperature of YSZ was specified as 2950 K (Ref 2) and the initial undercooling as 150 K; thus when the interface temperature at the melt/substrate interface initially reached 2800 K, grain growth began. Finally, we set the kinetic coefficient $\mu = 0.0012$ m s^{-1} K^{-1} (Ref 2).

As indicated in Fig. 3, the parabolic and hyperbolic equations yield very similar curves of interface velocity V_i during the early stages of solidification; the hyperbolic results always predict a slightly higher velocity, and the difference between the models is more pronounced for the higher value of h. However, compared to results obtained for pure metal solidification (Ref 5), the difference between the parabolic and hyperbolic models (Fig. 3) is actually more significant. With $h = 1.0 \times 10^7$ W m^{-2} K^{-1}, V_i increases sharply from 0.1 m s^{-1} to 0.8 m s^{-1} at the very beginning of solidification, before decreasing slowly. With $h = 5.0 \times 10^7$ W m^{-2} K^{-1}, the maximum velocity is 1.5 m s^{-1}, which is larger than V_D. These velocity curves are very similar to those obtained by Wang (Ref 2).

Profiles of interface temperature T_i are presented in Fig. 4, and again, the difference between results obtained by the parabolic and hyperbolic models is relatively small, although more pronounced at the higher value of h. With $h = 1.0 \times 10^7$ W m^{-2} K^{-1}, T_i decreases from 2850 K to 2250 K abruptly at the initial stage of solidification, before T_i plateaus. The variation of T_i when $h = 5.0 \times 10^7$ W m^{-2} K^{-1} is even more dramatic, as the temperature falls to about 1600 K before recovering. In both cases the rapid initial temperature decrease is related to the initially low interface velocity, which in turn implies a weak latent heat release; as V_i increases, the latent heat release becomes intense, and compensates for the heat loss to the substrate, which causes the temperature to stabilize. As for why the hyperbolic model yields temperatures that are lower than those obtained from the parabolic model, consider that interface velocity is related to undercooling; because the hyperbolic model predicts a higher interface velocity, the undercooling is greater, and so T_i is lower.

Figure 5 shows k_f versus location of the solidification front, and unlike the previous results, the parabolic and hyperbolic models yield dramatically different results. With $h = 1.0 \times 10^7$ W m^{-2} K^{-1}, the parabolic model predicts that k_f decreases from 1.9 to 1.7; the hyperbolic model predicts that k_f decreases to 1.3. Much more

Table 1 Physical properties of YSZ used in the calculations (Ref 2, 4, 22)

Parameter	Units	YSZ
T_0	K	3250
T_m	K	2950
D_L	m^2 s^{-1}	1.0×10^{-9}
D_S	m^2 s^{-1}	$\sim 10^{-15}$
k_e		2.1
κ_L	W m^{-1} K^{-1}	3
κ_S	W m^{-1} K^{-1}	2
C_{PL}	J kg^{-1} K^{-1}	713
C_{PS}	J kg^{-1} K^{-1}	580
ρ_L	kg m^{-3}	5890
ρ_S	kg m^{-3}	5890
m_e	K wt.%$^{-1}$	2.9
C_0	wt.%	8
Q	J kg^{-1}	8.12×10^5
V_D	m s^{-1}	1~2
μ	m s^{-1}K^{-1}	0.0012

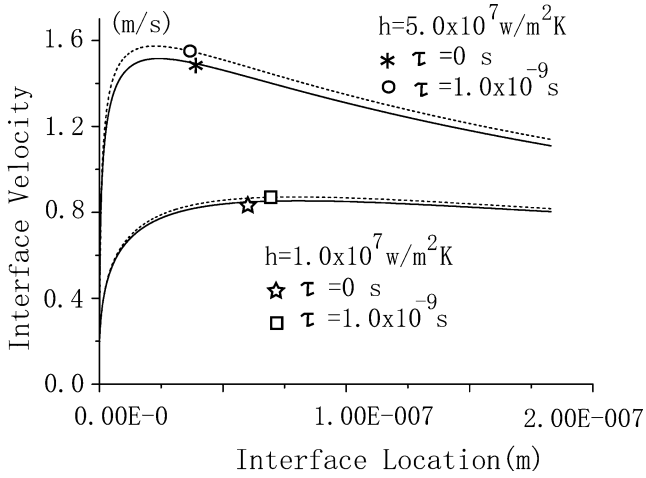

Fig. 3 Interface velocity versus interface location

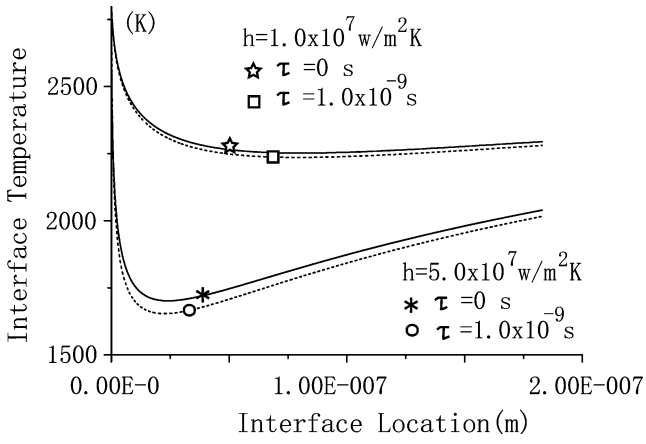

Fig. 4 Interface temperature versus interface location

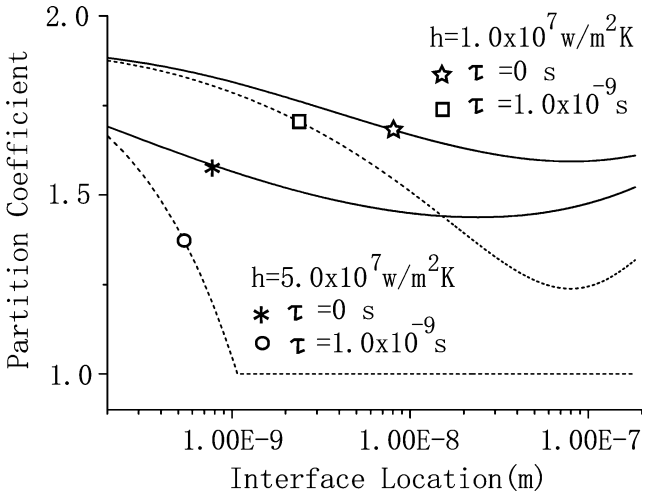

Fig. 5 Partition coefficient versus interface location

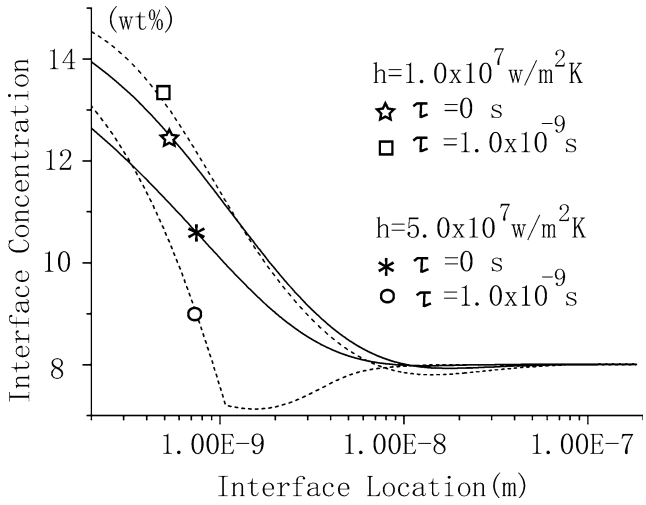

Fig. 6 Interface concentration at solid side versus interface location

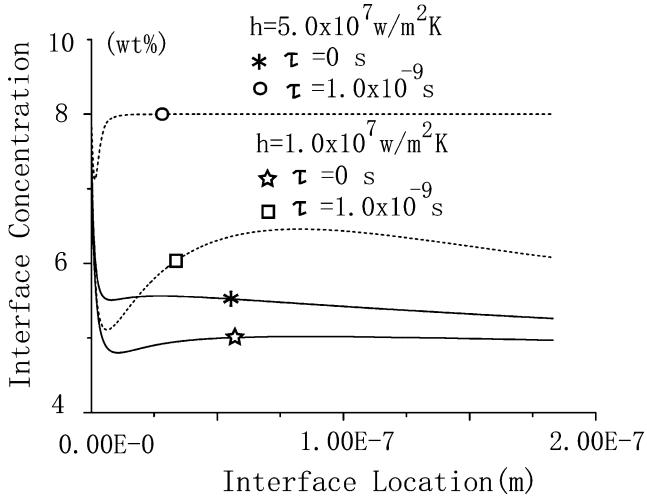

Fig. 7 Interface concentration at liquid side versus interface location

interesting is when $h = 5.0 \times 10^7$ W m^{-2} K^{-1}, because the hyperbolic model predicts a discontinuous variation of k_f, which quickly falls to 1, after which there is no segregation. The reason, according to Galenko's model (Eq 10, 13), is that $V_i \rightarrow V_D$ is a critical condition, because $k_f \rightarrow 1$ and concentration trapping begins. The parabolic model based on Aziz's equations, on the other hand, has no critical condition and so the curves are smooth. Finally, note that because the hyperbolic model predicts a higher V_i, it then approaches V_D more rapidly than the parabolic model.

Figure 6 presents C^+ (the yttria concentration on the solid side of the interface) versus location of the solidification front. At the very beginning of solidification, because the liquidus slope of YSZ is positive (according to the phase diagram), the partition coefficient is greater than 1 and so $C^+ > C_0$ for all results. With $h = 5.0 \times 10^7$ W m^{-2} K^{-1}, C^+ (predicted by both the parabolic and hyperbolic models) is lower than when $h = 1.0 \times 10^7$ W m^{-2} K^{-1}, because $k_f > 1$, and according to Eq 9, k_f decreases as V_i increases. When V_i is higher, segregation is lower, and therefore C^+ is lower. With $h = 5.0 \times 10^7$ W m^{-2} K^{-1}, the hyperbolic model yields a concentration that actually drops to a value less than C_0 before reaching a minimum; after this point, C^+ approaches C_0 when concentration is totally trapped. Finally, note that all of the curves show that C^+ approaches C_0 (8 wt.%) at steady state, which is evidence of mass conservation.

Figure 7 presents C^- (the yttria concentration on the liquid side of the interface) versus location of the solidification front. Both the hyperbolic and parabolic models predict C^- to be less than 8.0 wt.%. When $h = 1.0 \times 10^7$ W m^{-2} K^{-1}, C^- drops rapidly from 8.0 wt.% to a minimum value, then quickly approaches an equilibrium that depends on whether the parabolic or hyperbolic equations are being solved. The physical explanation for this phenomenon is as follows: at the beginning of solidification, because interface velocity is relatively low, the partition coefficient is relatively high, and so C^- decreases to maintain a higher concentration on the solid side. As V_i increases, the partition coefficient drops, and so C^- begins to rise. Also worth noting is that C^- rises faster with the hyperbolic model, because V_i is higher, and so C^- approaches steady state more quickly. When $h = 5.0 \times 10^7$ W m^{-2} K^{-1}, $V_i \rightarrow V_D$ and so solute is trapped, which explains why the hyperbolic curve shows that C^- rapidly equals C_0. Finally, note that the difference between the hyperbolic and parabolic curves of C^- is much more pronounced than the differences in the curves of V_i and T_i, and that the difference becomes larger as h increases.

The surface temperature beneath a splat will affect the strength of adhesion. Profiles of this temperature are presented in Fig. 8, and again, the difference between the parabolic and hyperbolic models is relatively small, although more pronounced at the higher value of h. With $h = 1.0 \times 10^7$ W m^{-2} K^{-1}, the temperature decreases

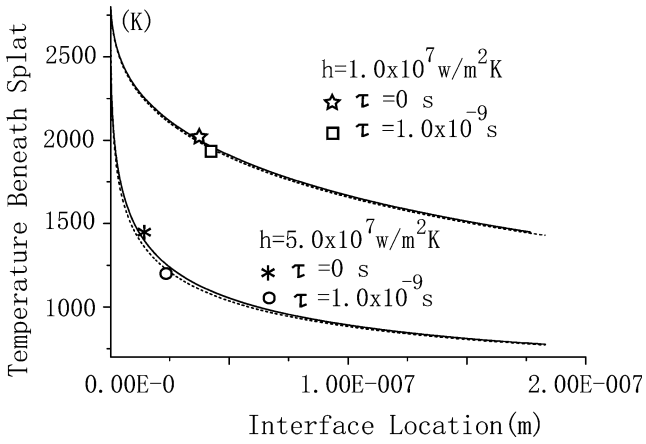

Fig. 8 Temperature beneath a splat versus interface location

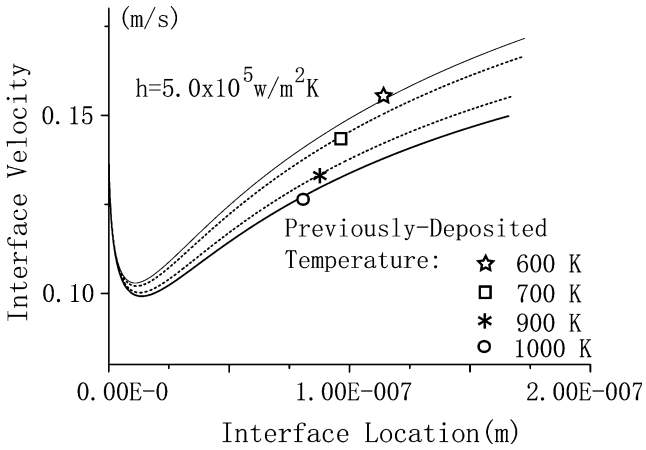

Fig. 9 Interface velocity versus interface location, for solidification onto a previously deposited splat

from 2850 K to 1500 K abruptly at the initial stage of solidification, and then plateaus. The variation of the temperature at $h = 5.0 \times 10^7$ W m^{-2} K^{-1} is even more dramatic, as the temperature immediately falls to about 700 K. Clearly the splat/substrate temperature is closely related to h. To obtain strong adhesion, the substrate surface is usually prepared before spraying, to get rid of surface contamination and oxidation. Those factors will strongly affect the heat transfer coefficient.

Finally, the results so far have considered a single splat solidifying on a stainless steel substrate. More generally, there are multiple layers of splats that fall upon each other, and the previously deposited splats can be either solid or liquid. To simulate the solidification of multiple splats, we assumed a previously deposited temperature in the range from 600 to 1000 K. The heat transfer coefficient was also assumed lower: $h = 5.0 \times 10^5$ W m^{-2} K^{-1}; this value was estimated based on the splat thickness and the heat conduction properties of YSZ (heat resistance into previously deposited YSZ will be far greater than that into a stainless steel substrate). The parabolic and hyperbolic equations yielded very similar curves of interface velocity V_i during the early stages of solidification, and so only the parabolic results are presented. Figure 9 illustrates that V_i decreases as the temperature of the previously deposited layer increases, and the differences between the V_i profiles are almost linearly related to the differences between temperatures of the previously deposited splats. Comparing this result to that of Fig. 3, V_i for multiple splat deposition is much smaller, and so the nonequilibrium behaviors are significantly less.

4. Conclusions

We have previously investigated nonequilibrium phase change during rapid solidification of a pure metal (Ref 5). In this work we considered a coupled set of hyperbolic equations for temperature and concentration. Using an interface tracking method, the model simulates 1D nonequilibrium phase change of a binary system effectively. YSZ was chosen for the simulation based on the relatively low magnitude of the diffusive speed. The results show that for a realistic relaxation time (10^{-9} s), the profiles of V_i and T_i versus interface location are significantly affected by h, while the effect of hyperbolic behavior is relatively minor. Only the interface concentration shows pronounced differences between the hyperbolic and parabolic models, and these become larger as h increases. Also, the hyperbolic model yields a turning point when $V_i \rightarrow V_D$, as the concentration on the liquid side of the solidification front is frozen or trapped. We also examined a droplet impacting onto a previously deposited splat; results show that V_i is lower because the heat transfer coefficient is presumed lower, and so nonequilibrium behavior is not obvious.

References

1. Y.K. Chae, J. Mostaghimi, and T. Yoshida, Deformation and Solidification Process of a Super-cooled Droplet Impacting on the Substrate Under Plasma Spraying Conditions, *Sci. Technol. Adv. Mat.*, 2000, **1**, p 147-156
2. G.-X. Wang, R. Goswami, S. Sampath, and V. Prasad, Understanding the Heat Transfer and Solidification of Plasma-sprayed Yttria-partially Stabilized Zirconia Coatings, *Mater. Manuf. Process.*, 2004, **19**, p 259-272
3. T. Streibl, A. Vaidya, M. Friis, V. Srinivasan, and S. Sampath, A Critical Assessment of Particle Temperature Distributions During Plasma Spraying: Experimental Results for YSZ, *Plasma Chem. Plasma Process.*, 2006, **26**, p 53-72
4. D.R. Clarke and C.G. Levi, Materials Design for the Next Generation Thermal Barrier Coatings, *Annu. Rev. Mater. Res.*, 2003, **33**, p 383-417
5. H. Liu, M. Bussmann, and J. Mostaghimi, A Comparison of Hyperbolic and Parabolic Models of Phase Change of a Pure Metal, in press, *Int. J. Heat Mass Tran.*, 2008. doi:10.1016/j.ijheatmasstransfer.2008.08.030
6. A.M. Mullis, Rapid Solidification Within the Framework of a Hyperbolic Conduction Model, *Int. J. Heat Mass Tran.*, 1997, **40**, p 4085-4094
7. S.L. Sobolev, Rapid Solidification Under Local Nonequilibrium Conditions, *Phys. Rev.*, 1997, **55**, p 6845-6854
8. P.K. Galenko and D.A. Danilov, Linear Morphological Stability Analysis of the Solid-Liquid Interface in Rapid Solidification of a Binary System, *J. Phys. Rev. E*, 2004, **69**, p 051608, 1-13

9. P.K. Galenko and D.A. Danilov, Local Nonequilibrium Effect on Rapid Dendritic Growth in a Binary Alloy Melt, *Phys. Lett. A*, 1997, **235**, p 271-280
10. L. Bianchi, F. Blein, P. Lucchese, M. Vardelle, A. Vardelle, and P. Fuchais, Effect of Particle Velocity and Substrate Temperature on Alumina and Zirconia Splat Formation, *Thermal Spray Industrial Applications*, C. Berndt and S. Sampath, Ed., (Materials Park, OH), ASM International, 1994, p 569-574
11. M. Fukomoto, Y. Huang, and M. Ohwatari, Flattening Mechanism in Thermal Sprayed Particle Impinging on Flat Substrate, *Thermal Spray Meeting the Challenges of the 21st Century*, C. Coddet, Ed., (Materials Park, OH), ASM International, 1998, p 401-406
12. M. Pasandideh-Fard, V. Pershin, S. Chandra, and J. Mostaghimi, Splat Shapes in a Thermal Spray Coating Process: Simulations and Experiments, *J. Therm. Spray Technol.*, 2002, **11**, p 206-217
13. W. Kurz and D.J. Fisher, *Fundamentals of Solidification*, 4th ed., Trans Tech Publications, Aedermannsdorf, 1998, p 63-89
14. G.-X. Wang and E.F. Matthys, Modeling of Nonequilibrium Surface Melting and Resolidification for Pure Metals and Binary Alloys, *J. Heat Transf.*, 1996, **118**, p 944-951
15. C. Li, J. Li, and W. Wong, The Effect of Substrate Preheating and Surface Organic Covering on Splat Formation, *Thermal Spray Meeting the Challenges of the 21st Century*, C. Coddet, Ed., (Materials Park, OH), ASM International, 1998, p 473-480
16. J. Pech, B. Hannoyer, A. Denoirjean, and P. Fauchais, Influence of Substrate Preheating Monitoring on Alumina Splat Formation in DC Plasma Process, *Thermal Spray Surface Engineering via Applied Research*, C. Berndt, Ed., (Materials Park, OH), ASM International, 2000, p 759-765
17. H.R. Salimi Jazi, J. Mostaghimi, T. Coyle, S. Chandra, C.Y. Lau, L. Rosenzweig, and E. Moran, Effect of Droplet Characteristics and Substrate Surface Topography on the Final Morphology of Plasma Sprayed Zirconia Single Splat, *J. Therm. Spray Technol.*, 2007, **16**, p 291-299
18. M.J. Aziz and T. Kaplan, Continuous Growth Model for Interface Motion During Alloy Solidification, *Acta Metall.*, 1998, **36**, p 2335-2347
19. M.J. Aziz and W.J. Boettinger, On the Transition from Short-range Diffusion-limited to Collision-limited Growth in Alloy Solidification, *Acta Metall. Mater.*, 1994, **42**, p 527-537
20. C. Cattaneo, Sulla conduzione del calore, *Atti Sem. Mat. Fis. Univ. Modena*, 1948, **3**, p 83-101
21. P.K. Galenko and D.A. Danilov, Model for Free Dendritic Alloy Growth Under Interfacial and Bulk Phase Nonequilibrium Conditions, *J. Cryst. Growth*, 1999, **197**, p 992-1002
22. H.-B. Xiong, L.-L. Zheng, and T.A. Streibl, Critical Assessment of Particle Temperature Distributions During Plasma Spraying: Numerical Studies for YSZ, *Plasma Chem. Plasma Process.*, 2006, **26**, p 53-72